Ruptures in Mixed Monolayers Under Tension and Supercooling: Implications for Plant Nanobubbles

Stephen Ingram,*,† Bernhard Reischl,† Timo Vesala,†,‡ and Hanna Vehkamäki*,†

†*Institute for Atmospheric and Earth System Research/Physics, Faculty of Science, P.O. Box 64, University of Helsinki, Helsinki, FI-00014 Finland*

‡*Institute for Atmospheric and Earth System Research/Forest Sciences, Faculty of Agriculture and Forestry, P.O. Box 27, University of Helsinki, Helsinki, FI-00014 Finland*

E-mail: stephen.ingram@helsinki.fi; hanna.vehkamaki@helsinki.fi

Abstract

Mixed phospholipid and glycolipid monolayers likely coat the surfaces of pressurised gas nanobubbles within the hydraulic systems of plants. The lipid coatings bond to water under negative pressure and are thus stretched out of equilibrium. In this work, we have used molecular dynamics simulations to produce trajectories of a biologically relevant mixed monolayer, pulled at mild negative pressures (−1.5 to −4.5 MPa). Pore formation within the monolayer is observed at both 270 and 310 K, and proceeds as an activated process once the lipid tails fully transition from liquid condensed/liquid expanded (LC/LE) coexistence to the liquid expanded phase. Pressure : area isotherms showed reduced surface pressure in the undercooled trajectory at all observed areas per lipid. Rayleigh-Plesset simulations were used to predict evolving nanobubble size using the calculated pressure : area isotherms as dynamic surface tensions. We confirm the

existence of a critical radius with respect to runaway growth, above the homogeneous cavitation radius, coinciding with the area per lipid at which pore formation occurs.

Introduction

Tree sap exists in a state some have described as "doubly" metastable:[1] liquid water is transported from root to leaf under negative pressure, and, in some climates, below its freezing point for much of the year.

In the tree science community, negative pressure is referred to as 'water potential' (per the Gibbs-Duhem equation, chemical potential per unit volume has the dimensionality of pressure) and arises from water being stretched away from its equilibrium density.[2,3] The entirety of the driving force for the stretching, and hence the upward flux of water against gravity, is produced by evaporation within confined channels on the leaf surface called stomata.[4] The magnitude of the negative pressure within the leaf tissue can be calculated using the Kelvin equation, by considering the water activity gradient directly above the leaf,[5,6]

$$\Psi_{\text{water}} = \Delta P_{\text{Leaf}} = \frac{RT}{V_{\text{m}}} \ln(a_{\text{w}}), \tag{1}$$

where V_{m} is the molar volume of water, and a_{w} is the ambient relative humidity at sufficient distance from the leaf surface. Water potential is therefore the most negative directly below the stomata, and it is only here that the first equality of Equation 1 holds. Further from the leaves, the magnitude of Ψ_{water} decreases (becomes less negative) and approaches a value of ΔP_{Root} at the external membranes of the roots.[4]

Sap water moves from root to leaf through rows of microscopic conduits, collectively called xylem. The xylem walls are reinforced with lignified material for rigidity, but also contain so-called pit membranes embedded into them. Pit membranes exhibit a partially porous structure, formed of overlapping lignin fibres[7,8] which allow lateral movement of water between conduits. If a single conduit has embolized, i.e. filled with gas, the combination of

(positive) gas pressure on one side of the pit with liquid under negative pressure on the other will extrude nanobubbles through the porous mesh, and into the bulk liquid.

It has become clear in recent years that pit membranes are coated with large concentrations of lipids, in either monolayer or micellar form.[9] Lipid composition within the xylem sap water itself has also been studied, via mass spectrometry, in several species of tree.[10] While the ratios of specific lipids varied, phospholipids tended to dominate, with glycolipids and triglycerides appearing at lower concentrations. Any air nanobubbles seeded through a pit membrane will therefore be coated with a monolayer of surfactants during the formation or "budding off" process. These coatings have also been observed within cryo-SEM images of frozen xylem sap samples.[11]

The internal (positive) pressure of gas that can exist inside a nanobubble at equilibrium is determined by the Laplace equation:

$$\Delta p_{\text{Laplace}} = \frac{2\gamma}{r} \tag{2}$$

Depending on the surface tension, γ, exhibited, equation 2 predicts that a bubble of radius $r = 50$ nm could sustain a pressure differential across its interface of between 1.8 and 2.7 MPa, corresponding to the observed bulk xylem surface tension range of 45 and 68 mNm^{-1} respectively.[12] Due to the direction of the applied force, a surrounding water potential of $\Psi_{\text{water}} = -1$ MPa would lower, rather than raise, the internal bubble pressure, to 0.8 – 1.7 MPa. As described above, this effect would become more pronounced closer to the leaves, as the contribution of Ψ_{water} to $\Delta p_{\text{Laplace}}$ becomes more significant.

However, these surface tensions are bulk values that do not take into account that the concentrations of lipids at the bubble surface will be significantly higher than within the xylem sap as a whole. Furthermore, γ itself is not static with respect to either radius or the physical conditions the bubble experiences. It must be represented by a full pressure area isotherm, dependent on both Ψ_{water} and temperature.

To our knowledge, there has been no investigation into the effect of temperature on mixed monolayers containing glycolipids and phospholipids. Majewski et al.[13] found that doping a DPPC monolayer with up to 20 mole% of the glycolipid GM1 had little impact on the pressure area isotherms at a temperature of 23°C, despite monolayers of the pure glycolipid having a much broader and shallower increase in surface pressure during compression. The same system was investigated by Frey et al.[14] with a larger range of mixing ratios, who found that small amounts of glycolipid have a condensing effect on the monolayers, and only deviate significantly from the pure DPPC dependence at an above 50 mole% GM1. Unfortunately, neither of these lipids occur in tree sap, nor do these studies offer insight into the behavior of monolayers under supercooled or negative pressure conditions.

In our previous work,[15] we calculated dynamic surface tensions of a prototypical glycolipid as a function of applied negative pressure. A kinetic effect was observed where larger pulling rates reduced the surface pressure, Π_{MD}, as the interface expanded faster than the lateral diffusion of the lipids could compensate. Conversely, a monolayer comprised of a prototypical phospholipid was found to rapidly condense into a stable lamellar-like liquid condensed (LC) phase, rendering it highly resistant to pulling, even for pressures as negative as -3.5 MPa.

These results emphasize that the instantaneous surface tension of a nanobubbles coating determines not only the pressure differential it can sustain, but also its stability with respect to embolising the conduit it is in. Here we wish to increase the complexity of the studied system by (1) introducing two component monolayers, (2) varying the temperature within biologically relevant bounds, and (3) increasing the (positive) gas pressure to be in line with that predicted by equation 2 for tree nanobubbles under negative liquid pressure.

We have utilised molecular dynamics simulations to investigate mixed monolayers of phospho- and glycolipids, using the CHARMM36 biomolecular force field. Plant lipids generally possess polyunsaturated tail groups,[16] and therefore exhibit low 'melting points' (LC/LE transition temperatures). In recognition of this, we have specifically used dilinoleoyl-phosphatidylethanolamine (DLiPE 18:2/18:2) and digalactosyl-diacylglycerol (DGDG 18:3/16:3)

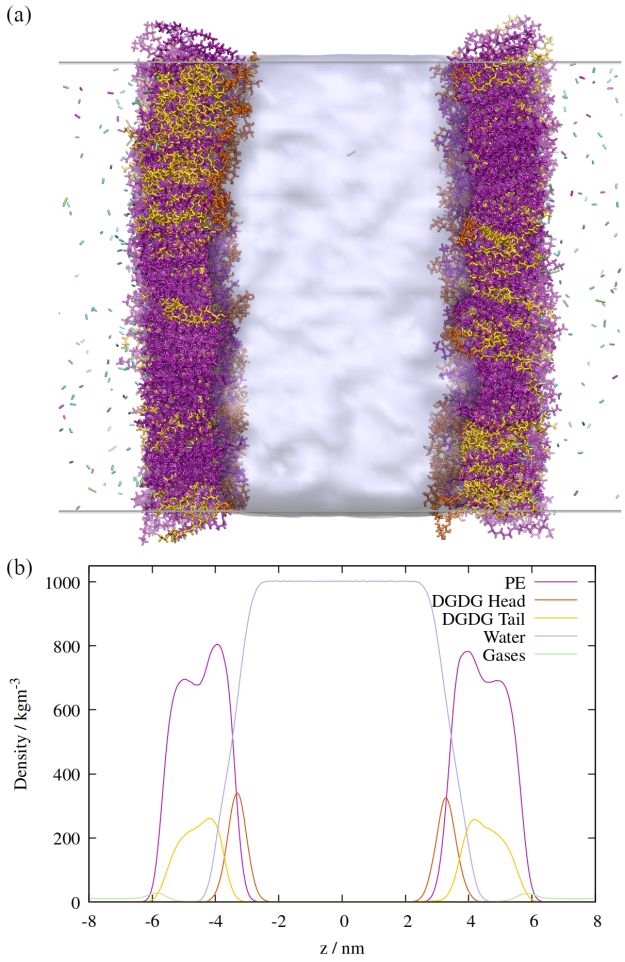

Figure 1: (a) Side view of the atomistic model of the double interface of a gas bubble-lipid monolayer-water system, investigated at an area of 0.55 nm^2 per lipid. Lipid and gas molecules are shown in licorice representation with PE in purple, DGDG in orange (head) and yellow (tail). The surface of the water volume is shown in light blue. Note that the two gas volumes on either end of the simulation box are connected through periodic boundary conditions and constitute the "inside" of the bubble, whereas the water volume in the center of the box represents the liquid surrounding the bubble. (b) Density profiles of the system components across the two interfaces, averaged over a 60 ns molecular dynamics trajectory.

in this study. To avoid confusion with dilauroyl-phosphatidylethanolamine (DLPE) the phospholipid will be referred to hereinafter by the more general term PE, as this is how it is named in the tree science community. We have represented the PE head group as zwitterionic as, at the close to neutral pH of xylem sap, phosphate groups will be deprotonated and ammonium groups will be protonated.[11,17]

An orthographic projection of the system viewed along the x dimension is shown in Figure 1, along with the associated lateral densities of the components after equilibration. The mixing ratio was 3:1 PE:DGDG by number and there were 300 lipids in each monolayer. Such a ratio reflects the general trend in sap concentrations of the two lipid types, although compositions vary substantially from species to species.[9]

The Kirkwood-Buff method of calculating surface tension from molecular dynamics simulation,

$$\gamma_{\mathrm{MD}} = \frac{L_z}{2}[P_z - P_{xy}], \tag{3}$$

describes that the presence of an interface between two phases will induce a difference in pressure between the in plane (P_{xy}) and out of plane (P_z) dimensions of the surface. In atomistic simulations, there are usually two interfaces present: the top and bottom of a liquid slab, placed within a box of vertical size L_z. Note that the above equation was derived from consideration of a system in which the mean distance between interfaces does not change over the timescale probed.[18] Therefore, constant volume simulations containing high Laplace pressures of gas in contact with the lipid interfaces are most likely to give accurate results in this context.[19]

Results and discussion

First, a series of lateral pulling trajectories were conducted in the NpT ensemble, at T = 270 K and 310 K. We believe these to be reasonable upper and lower limits for the temperatures experienced by the hydraulic systems of most vascular plants. 270 K is substantially

above the melting point of our water model (252 K for TIP4P/2005[20]), meaning the system exhibited the correct thermal energy of supercooled water, without the risk of ice nucleation occurring within the simulation. It is also consistent with the phenomenon under study: sap present in xylem conduits can often withstand supercooling down to −10°C before freezing.[1]

Increasingly negative pressures were applied in the xy plane, in increments of 20 ns, to induce expansion of the mean area per lipid (APL). In contrast to the pure phospholipid system investigated in our previous work, expansion of the mixed monolayer occurred relatively rapidly at both temperatures studied. More extreme pulling rates induced faster expansion and the system plateaued at a more stretched configuration relative to the starting coordinates.

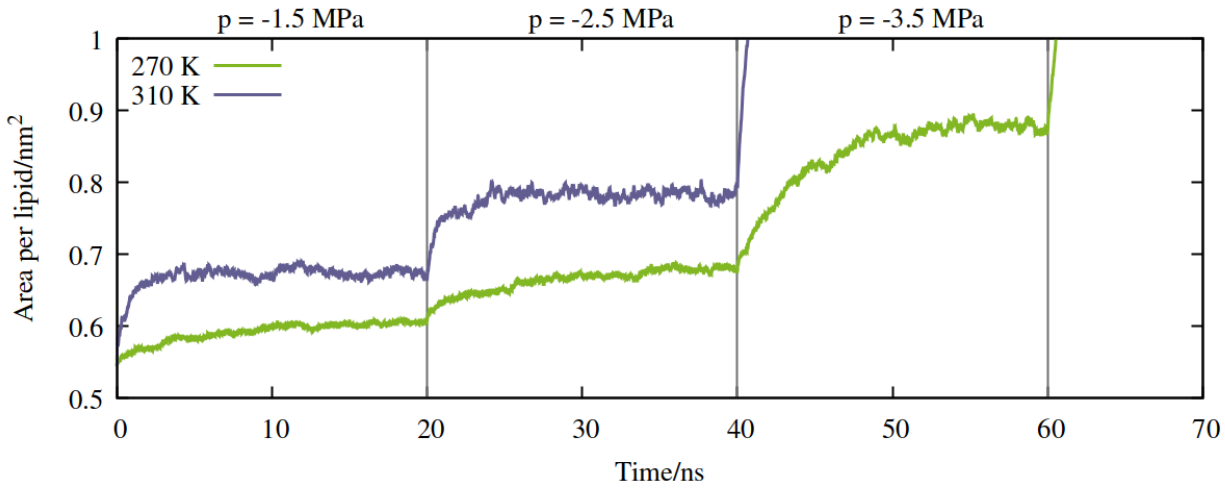

Figure 2: Expansion of the mixed monolayer during sequential pulling simulations, with increasingly negative pressure p, at $T = 270$ K (green) and 310 K (blue).

Figure 2 shows the 270 K system adopting larger equilibrium APL values during the first three NpT simulations, corresponding to pressures of −1.5, −2.5 and −3.5 MPa, respectively. Approximately 2 ns into the fourth trajectory, under a pressure of −4.5 MPa (t = 62 ns in Figure 2), both monolayers lost all structural integrity and underwent runaway growth. The 310 K system expanded faster, suffering a similar fate during the −3.5 MPa simulation: Somewhat counter-intuitively, the monolayer in the doubly metastable state (negative pres-

sure + supercooling) was more stable with respect to rupture than in the singly metastable state.

Since pore formation is an activated process in self assembled lipid nanostructures,[21,22] it requires both thermal energy and pulling to occur at high probability within a single MD trajectory. A deficit in one (a lower temperature) must be made up for by the other (a more negative pressure).

Temperature dependent surface tension

Directly calculating the surface tension of the evolving monolayer as a function of area within NpT simulations is undesirable because, as described earlier, the interlayer distance varies over time. Therefore, to produce pressure : area isotherms across the APL range traced by the above trajectories, a total of 44 frames were selected, between 0.55 and 1.20 nm^2 per lipid (23 frames for 270 K, 21 frames for 310 K). Each area was then simulated for 60 ns in the NVT ensemble, with the x, y and z components of the pressure tensor output every 2 ps. The first 10 ns was removed from the analysis, to allow the newly randomized velocities to decorrelate from their initial states.

The APL = 0.55 nm^2 per lipid configuration was considered close to the equilibrium density at 270 K as, by virtue of the compression steps during equilibration, it was the only frame for which the lateral components of the pressure tensor were positive. Conversely, at 310 K, the monolayer expanded from 0.55 to 0.57 nm^2 per lipid within the first 20 ps of the first pulling trajectory, and remained there for approximately 100 ps. This suggested that 0.57 nm^2 per lipid was the closest to completely stabilised interface that could be sustained at the higher temperature, and simulation of less expanded configurations would result in a negative surface tension. The trend in calculated surface tensions bears this assumption out.

The shape of the pressure : area isotherms (Figure 3, panel a) are as expected between 0.55 and 0.88 nm^2 per lipid, namely they show a collapse towards zero as the expansion

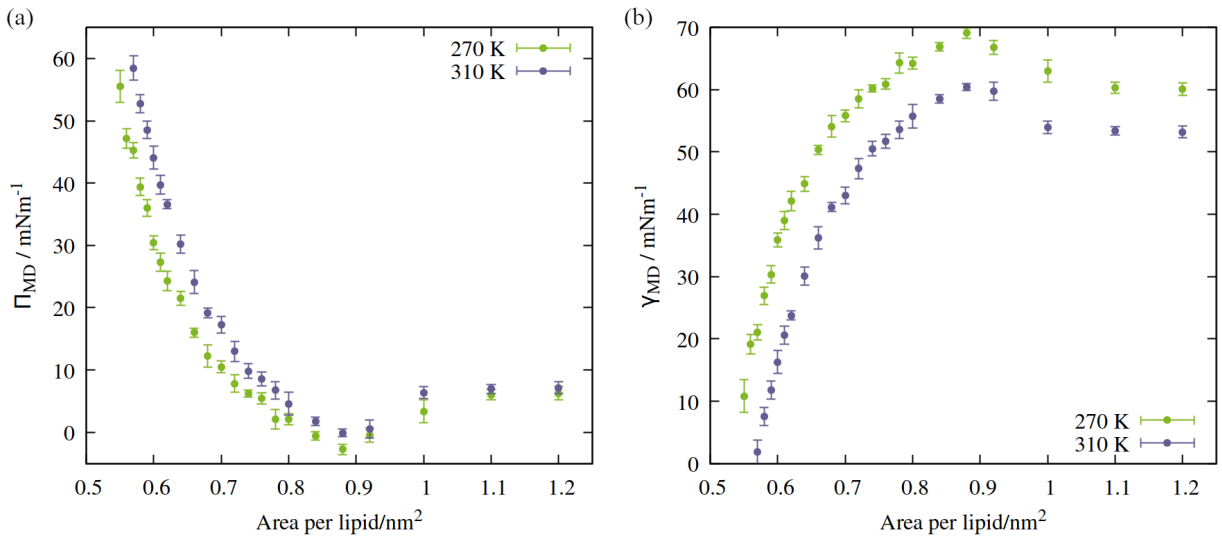

Figure 3: Isotherms showing (a) surface pressure, and (b) surface tension as a function of the area per lipid within the studied mixed monolayer at temperatures $T = 270$ K (green) and 310 K (blue).

proceeds and the outward force exerted by the monolayer on the periodic boundary decreases. Within this area range, the surface tension γ_{MD} was larger at 270 K than 310 K and the surface pressure Π_{MD} was lower: the thermal energy of the system was smaller relative to the surface free energy, meaning that the energetic cost of expanding the area was increased, by between 10 and 15 mNm^{-1}.

The surface tension of the interface slightly exceeded that of the pure water model at $T = 270$ K and APL $= 0.88$ nm^2, leading to a single negative surface pressure value. As we will see later, this inflection point corresponds to the largest area the monolayer can sustain before pore formation occurs. The mean values of P_{xy} for the two simulations conducted at this area were -2.90 MPa at 270 K and -3.47 MPa at 310 K, meaning the latter was in a close to critical configuration, near its rupture point, during the third NpT simulation (Figure 2).

In other words, a larger surface tension at the critical area corresponds to a more negative ambient value of P_{xy} that can be sustained without rupturing. To draw an analogy with the plant hydraulic system, bubble surfaces resembling those investigated here will be more

stable with respect to embolism at lower temperatures, both at a given negative pressure, Ψ_{water}, and across a wider range. This result is consistent with some previous tree level experiments; Cochard et al.[23] produced negative pressures in cut branches using a centrifuge, at temperatures between 50 and 1°C. They found that cooling the branches made them more resistant to embolism at a given negative pressure.

However, it is difficult to generalise from experiments where p and T are varied independently: they are correlated within the plant hydraulic system and change in a complex and path dependent manner. For example, increased temperatures can reduce soil water content, stressing plants and increasing the negative pressures within them. Other environmental factors can affect Ψ_{water} on both a diurnal and annual timescale, such as ambient relative humidity, per Equation 1, or the rate of photosynthesis throughout the day. These feedback loops make it difficult to infer a causal relationship between quantities like surface tension and the macroscopic rate of embolism.

Lipid phase characteristics

A script was written to classify the two dimensional phases of the monolayer lipids using a Voronoi tessellation of the sixth atoms in each of the lipid chains (further information provided in Methods). The proportion of atoms in the liquid condensed phase across the APL range is shown in Figure 4, panels a and d. Once the monolayers began to rupture, the largest pore radius was also calculated for the same frames. As expected, a sequential coexistence of phases is observed as the monolayer is pulled apart: The initial proportion of lipids in the LC phase at an area per lipid of 0.55 nm^2 was $24 \pm 1.4\%$. During subsequent pulling, the LC-LE coexistence region monotonically becomes an entirely LE leaflet, which then ruptures at further expansion, becoming LE-G (or LE+Pore).[19] The lipids reorganise cooperatively, and diffuse laterally at the same rate, although DGDG tail atoms were rarely found in the LC phase. This is likely a consequence of the additional double bond in both tail groups reducing packing efficiency.

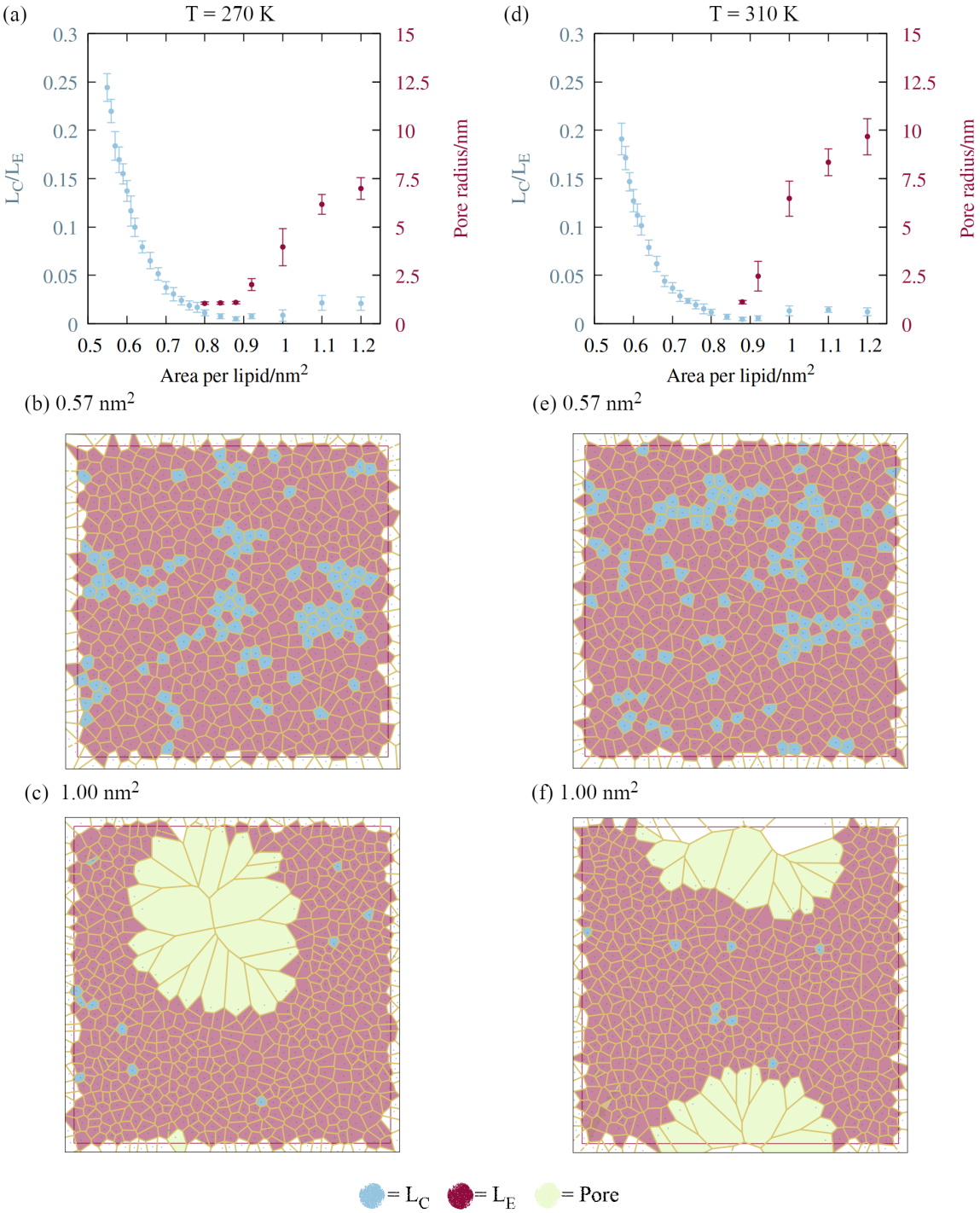

Figure 4: The impact of monolayer expansion on the phase state of the lipid tails at the two temperatures studied. (a) Reduction in the amount of liquid condensed phase (blue points) and increase in mean pore size (red points) at $T = 270$ K. Error bars represent standard deviations between $t = 10$ and 60 ns. Voronoi tessellations of lipid tail atoms at $t = 60$ ns are presented for areas per lipid of (b) 0.57 and (c) 1.00 nm^2, colored according to phase state. Panels (d),(e) and (f) follow (a),(b) and (c) for $T = 310$ K.

The lower contact between the tail groups at higher APL values can also be seen in the radial distribution functions (Figure S1). The correlation within the first solvation shell becomes smaller as the interfacial area increases. Peaks at lateral distances above 1 nm disappear at APL values of 0.88 nm^2 and above, corresponding to the transition of all tail groups out of the LC phase. Additionally, the rdf lineshape changes above 1.00 nm^2, as the finite size of the periodic boundary causes the long range correlation of the tails within the remaining leaflet to slightly increase.[24] Voronoi tessellations showing this effect are presented in Figure 4, panels c and f.

Inspection of the trajectories at APL = 0.92 nm^2 showed that, at both temperatures, only one of the two monolayers had ruptured, and this occurred during the simulation. Snapshots of the two trajectories at $t = 60$ ns are presented in Figure 5, showing pore formation within the 'upper' monolayer at 270 K and the 'lower' at 310 K, confirming the stochastic nature of the process. Glycolipids seem to be over-represented at the pore edges, suggesting, as above, that DGDG tails are less strongly bonded to their neighbors. Density iso-surfaces of the water slab show that the water level within the stable pores is slightly closer to the gas phase than the slab underneath the membrane, i.e. it rushes to occupy the center of mass of the monolayer.

Rayleigh-Plesset Dynamics

The molecular dynamics simulations reported above describe the properties of flat mixed monolayers, pulled by forces normal to the plane of the interface. We have produced an essentially two dimensional model of surface tension $\gamma_{MD}(APL)$, that cannot, as such, predict the evolving dynamics of a spherical interface under negative pressure. An approach is required which extends the Laplace equation 2 out of equilibrium and allows bubble radii to vary over time, $r(t)$, as a result of imbalances in the forces acing on their lipid coatings.[11]

In our previous work,[15] we showed that a nanobubble under tension sits in a potential well between two maxima: one occurs at the critical radius with respect to dissolution ($r \to 0$)

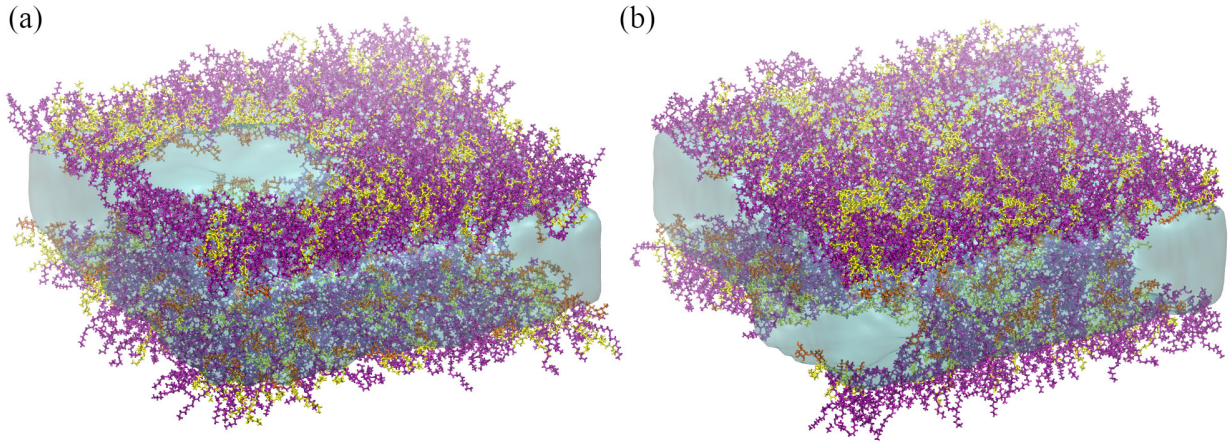

Figure 5: Snapshots of the final frame of the two NVT ensemble trajectories conducted at an area per lipid of 0.92 nm^2, at temperatures (a) $T = 270$ K and (b) $T = 310$ K. Water and lipid molecules are colored as in Figure 1, gas molecules are not shown.

and the other at the critical radius to embolism ($r \to \infty$). The stationary points can be identified by differentiating the Gibbs free energy of a bubble with respect to radius, to produce

$$\frac{dg(r)}{dr} = 8\pi r\gamma(r) + 4\pi r^2(p + \gamma'(r)). \tag{4}$$

The first critical radius can be identified by assuming it takes place at a size where the surface tension is static rather than dynamic, i.e. $\gamma'(r) = 0$. In this limit, the Laplace equation 2 is immediately recovered, as is the well-known Classical Nucleation Theory activation barrier height for cavitation of a void within liquid water,[25]

$$\Delta g_{\mathrm{CNT}}(r_{\mathrm{cavitation}}) = \frac{16\pi\gamma^3}{3p^2}. \tag{5}$$

Conversely, the equilibrium radius and the critical radius with respect to embolism both occur in the regime where surface tension is dynamic, meaning they are solutions to the full differential equation 4. The time dependent size of a bubble subject to this potential energy

surface should then follow the Rayleigh-Plesset equation of motion:[26,27]

$$\frac{dr(t)}{dt} = -\frac{r(t)}{4\eta}\left[p + \frac{2\gamma(r(t))}{2\delta + r(t)} + \gamma'(r(t))\right], \tag{6}$$

where η is the viscosity of water, and δ is the Tolman length, a measure of the curvature dependence of γ. There is little consistency in the literature as to the sign δ should adopt, but it is generally considered to be sub-nm or sub-Å in magnitude,[28] meaning the correction will be minimal at the r range studied here. A literature review revealed that different values of δ have been calculated for nucleating bubbles,[29] lipid monolayers[30] and water under negative pressure.[2] Here we have used a positive value, one tenth the Lennard Jones diameter of our water model, i.e. $\delta = +0.0316$ nm, proposed for bubbles under negative pressure by Kashchiev.[31]

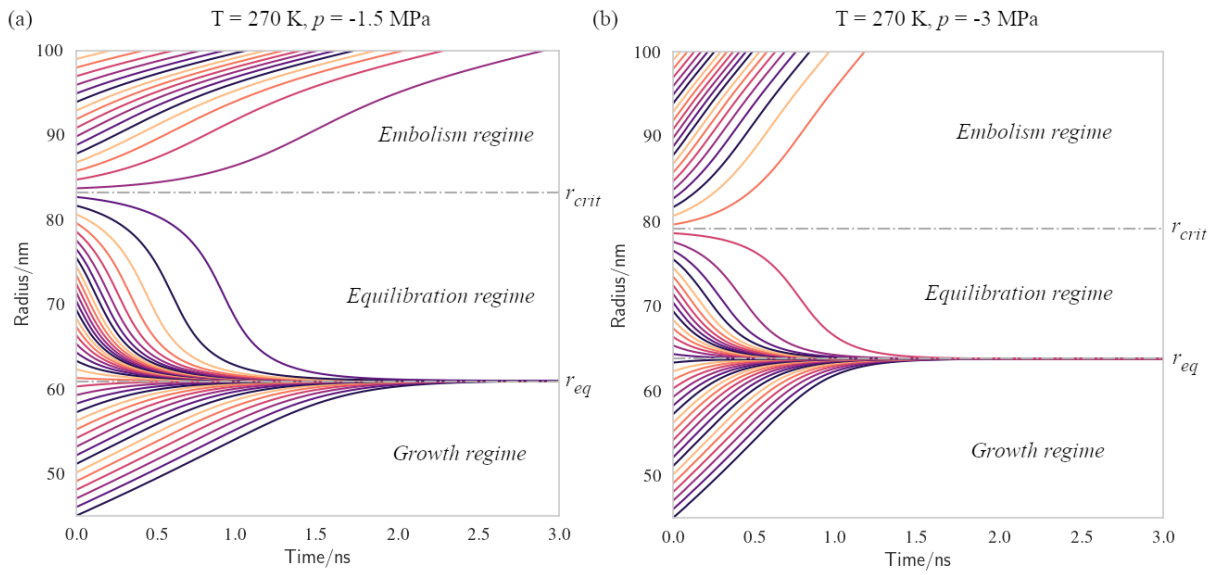

Figure 6: Bubble dynamics produced by integration of the Rayleigh-Plesset equation (Eq. 6), assuming $N_{\text{lipids}} = 10^5$, $T = 270$ K, and (a) $p = -1.5$ MPa, or (b) $p = -3$ MPa. Each panel contains 55 scans initialised at radii equally spaced between 45 and 100 nm. Further details in main text and Methods.

Given that the surface tension and external pressure are interrelated through both equations 2 and 3 (assuming $p = P_{xy}$), it should be noted that the sum of the first two terms

within the bracket in equation 6 are equal to the internal pressure within the nanobubble.

We have produced trajectories by numerically integrating equation 6, in the doubly metastable supercooled + negative pressure state, and $N_{\text{lipids}} = 10^5$. The large number of lipids was used to bring the equilibrium radius, r_{eq}, in line with that observed with nanoparticle tracking analysis of xylem nanobubbles by Guan et al.,[32] namely between 50 and 100 nm. The γ_{MD} values were smoothed to produce $\gamma(r)$ using a sum of two error functions. Scans of radius space were produced ranging from below r_{eq} to above the potential energy maximum (Figure 6).

The dynamics conform to three broad regimes which we call growth, equilibration and embolism. Bubbles injected below r_{eq} exhibit $\gamma(r)$ values close to zero and so dr/dt is strongly positive, leading to growth until the forces balance. Between r_{eq} and a second turning point, which we call r_{crit}, $\gamma(r)$ is highly dynamic and so $\gamma'(r)$ is maximised in this regime. A disequilibrium exists where the inward forces acting on the interface dominate the outward, and bubble size is spontaneously reduced. Among the bubbles that equilibrate, there is no further fluctuation in size, as the small thermal noise and viscosity damp any further motion. The activation barriers to embolism and dissolution are essentially insurmountable and the bubble size is stable, at least at this level of theory.

Above r_{crit}, the prefactor $-r/4\eta$ is maximised and $\gamma'(r)$ is small and negative, as this regime corresponds to areas per lipid within the monolayer coating above which pore formation and subsequent rupture happen. We note that r_{crit} is strictly the critical radius with respect to embolism and is therefore separate from $r_{\text{cavitation}}$, and only arises because $\gamma'(r) \neq 0$. Doubling the applied negative pressure from $p = -1.5$ MPa to -3 MPa (Figure 6b) leads to an increase in r_{eq} (the equilibrium APL becomes more stretched) but a decrease in r_{crit} (bubble volume must be smaller for the volumetric work pV to remain constant). In the limit of extreme negative pressure, r_{eq} and r_{crit} merge and both disappear: no equilibration regime is observed and all bubbles above $r_{\text{cavitation}}$ embolise, as the volumetric work dominates the dynamics (see Figure S2).

As there is no representation of gas or lipid diffusion towards the expanding interface in this model, or any kinetic limitation this might impose on bubble growth or shrinkage, the timescales over which these dynamics manifest are largely arbitrary and not representative of a chemically realistic system. We consider this a sensitivity study and the trajectories indicative of the 'fastest possible' direction of travel across the potential energy surface (Equation 4) the bubble experiences.

Conclusion

The role played by nanobubbles in the plant hydraulic system is beginning to come into sharper focus. Predicting under which physical conditions they will expand into embolism is of extreme importance, and requires a rigorous understanding of their surface coatings. By producing pressure area isotherms of a biologically relevant lipid monolayer, we have shown the range of surface tensions possible at both temperate and undercooled conditions. The occurrence of the LC phase within the studied monolayer was found to be initially low (ca. 25%) due to the polyunsaturated nature of plant lipid tails, and reduced monotonically as the area increased. Once the monolayer fully expanded into the LE phase, pore formation, followed by rupture, occured. A more negative pressure was required to induce rupture in the undercooled monolayers, a result that is consistent with observations of hydraulic stability in xylem conduits.

Nanosecond timescale Rayleigh-Plesset simulations show that the equilibrium radius of a bubble is largely determined by the number of lipids present in its coating. Bubbles formed above their equilibrium radius (i.e. with an expanded monolayer) were found to sometimes embolise, depending on the interplay between T, p and starting radius. This method can be used to estimate critical radii with respect to embolism, as well as the response of bubble size to changes in the conditions they experience.

Additional physics, such as Brownian motion or gas diffusion towards the bubble interface,

should be added in order to simulate dynamics at a timescale closer to that observable by experiment. It is also desirable to investigate the surface properties of other relevant lipids, as well as non-lipid surfactant classes present in plants, such as triacylglycerides[11] or denatured proteins.[33]

Methods

Two monolayers of 300 lipids were represented by the CHARMM36 force field, and the initial configurations generated using the CHARMM-GUI interface,[34] with initial areas per lipid specified as 50 $Å^2$ for PE and 75 $Å^2$ for DGDG. The number of water molecules within the slab was specified to be approximately 60 per lipid, and a total of 38711 molecules were generated. These were initially generated as TIP3P molecules, which were then converted to the TIP4P/2005 model[20] by adding an additional dummy atom at the same location as the second hydrogen atom of each molecule. As the dummy atom had no mass, it did not 'collide' with the H atom and so moved to the correct position when a steepest descents minimization was applied with the appropriate water model topology. The resultant monolayer configurations were then equilibrated in the NpT ensemble at 290 K, in six steps, using distance restraints that loosened progressively.

To produce the input coordinates for the pulling simulations, the gas phase was then populated with molecules using the GROMACS insert-molecules command. Van der-Waals radii were scaled to be twice their initial value to prevent gas molecules being inserted inside the monolayer or the water slab. The composition was calculated using the corrected ideal gas law for each species, with target pressures of 0.8 MPa N_2, 0.1 MPa O_2 and 0.1 MPa CO_2. The numbers of molecules are as follows: 766 N_2, 96 O_2 and 96 CO_2. CO_2 was represented by the flexible angle EPM2 model[35] and N_2 and O_2 by the rigid models described by Vujić and Lyubartsev.[36]

All simulations were performed on the Puhti cluster operated by CSC, utilizing a con-

figuration of 32 CPU cores and a single Nvidia v100 GPU. The GROMACS version was 2021.5.[37] The Nosé-Hoover expanded ensemble thermostat[38] was used for all pulling and 'production' isotherm simulations. Solvent, monolayer and gas groups were coupled to separate heat baths, each with a time constant of 0.75 ps. The Parrinello-Rahman barostat[39] was used for the pulling simulations, with a time constant of 5 ps and a lateral compressibility of 5×10^{-6} bar^{-1}, per Duncan and Larson.[40] The Verlet list, Van der Waals and Coulombic cut-offs were all set to 1.4 nm. Long range electrostatics were calculated using the particle mesh Ewald method, with a fourier spacing of 0.175 nm.

Surface tensions were converted to surface pressures according to the equation

$$\Pi_{\mathrm{MD}}(T) = \gamma_{\mathrm{water}}(T) - \gamma_{\mathrm{MD}}(T),$$

where the temperature dependent pure TIP4P/2005 surface tensions, $\gamma_{\mathrm{water}}(T)$, were taken from the parametrisation produced by Wang et al.[41] The LINCS algorithm[42] was used to constrain all bonds containing hydrogen atoms, with an order of 4 in the coupling matrix expansion, and a single iteration in the final step.

The Voronoi tessellations presented in Figure 4 were produced using the Voronoi library within the SciPy python module, with the mdtraj module[43] used to load the trajectories and select the appropriate atoms. The position data for both monolayers in each simulation were extracted every 2.5 ns, with the first 10 ns excluded. The periodic boundary was reconstructed by identifying the 'outer' tail group atoms as those whose polyhedra contained vertices outside the periodic box. The xy positions of these atoms were then translated by one box-width in both dimensions and were then appended to the input coordinates, at which point the Voronoi tessellation was recalculated. Tail group atoms were classified as being in the liquid condensed phase if they had six or more neighbors within 0.8 nm, at the pore edge if at least one vertex of the polyhedron was over 1.2 nm away from its center, and in the liquid expanded phase otherwise. The pore radii were calculated using the largest

distance between a series of grid points and their nearest atom in the xy plane, using the same atoms as the Voronoi tessellations. A similar procedure has been described in three dimensions for cavitation simulations by Gonzalez et al.[44] A grid size of 20×20 was used.

Equation 6 was integrated using the variable coefficient ODE solver in SciPy, with the backward differential formula method and a timestep of 1 ps. $\gamma(r)$ was represented by fitting a sum of two error functions to the data in Figure 3b, with $r = \sqrt{(APL \cdot N_{\text{Lipids}})/4\pi}$. The viscosity of water, η, was calculated as 2.00 $\times 10^{-3}$ Pa $\cdot$ s at 270 K using the parametrisation of Dehaoui et al.[45] Thermal noise was added as described in Menzl et al.,[25] according to the formula $\xi(t)\sqrt{k_{\text{B}}T/(8\pi\eta r)}$, where $\xi(t)$ samples from a gaussian distribution with a unit standard deviation, centered at zero.

Acknowledgement

SI and TV were funded by the Academy of Finland Consortium grant no. 342930 "The Hidden Role of Gases in Trees". BR and HV were funded by the Academy of Finland Centre of Excellence "VILMA - Virtual Laboratory for Molecular Level Atmospheric Transformations". Computational resources were provided by CSC-IT Centre for Science, Ltd., Espoo, Finland. The authors would like to thank Matti Javanainen for useful discussions.

Supporting Information Available

Supporting Information is available at dx.doi.org/10.XXXX

References

(1) Lintunen, A.; Hölttä, T.; Kulmala, M. Anatomical regulation of ice nucleation and cavitation helps trees to survive freezing and drought stress. *Scientific Reports* **2013**, *3*, 1–7.

(2) Azouzi, M. E. M.; Ramboz, C.; Lenain, J.-F.; Caupin, F. A coherent picture of water at extreme negative pressure. *Nature Physics* **2013**, *9*, 38–41.

(3) Singraber, A.; Morawietz, T.; Behler, J.; Dellago, C. Density anomaly of water at negative pressures from first principles. *Journal of Physics: Condensed Matter* **2018**, *30*, 254005.

(4) Wheeler, T. D.; Stroock, A. D. The transpiration of water at negative pressures in a synthetic tree. *Nature* **2008**, *455*, 208–212.

(5) Vera, F.; Rivera, R.; Romero-Maltrana, D.; Villanueva, J. Negative Pressures and the First Water Siphon Taller than 10.33 Meters. *PLOS ONE* **2016**, *11*, e0153055.

(6) Vincent, O.; Szenicer, A.; Stroock, A. D. Capillarity-driven flows at the continuum limit. *Soft Matter* **2016**, *12*, 6656–6661.

(7) Myburg, A. A.; Lev-Yadun, S.; Sederoff, R. R. Xylem Structure and Function. *eLS* **2013**, 1–19.

(8) Venturas, M. D.; Sperry, J. S.; Hacke, U. G. Plant xylem hydraulics: What we understand, current research, and future challenges. *Journal of Integrative Plant Biology* **2017**, *59*, 356–389.

(9) Schenk, H. J.; Espino, S.; Romo, D. M.; Nima, N.; Do, A. Y.; Michaud, J. M.; Papahadjopoulos-Sternberg, B.; Yang, J.; Zuo, Y. Y.; Steppe, K.; Jansen, S. Xylem Surfactants Introduce a New Element to the Cohesion-Tension Theory. *Plant Physiology* **2017**, *173*, 1177–1196.

(10) Schenk, H. J.; Michaud, J. M.; Mocko, K.; Espino, S.; Melendres, T.; Roth, M. R.; Welti, R.; Kaack, L.; Jansen, S. Lipids in xylem sap of woody plants across the angiosperm phylogeny. *The Plant Journal* **2021**, *105*, 1477–1494.

(11) Ingram, S.; Jansen, S.; Schenk, H. J. Lipid-Coated Nanobubbles in Plants. *Nanomaterials* **2023**, *13*, 1776.

(12) Losso, A.; Beikircher, B.; Dämon, B.; Kikuta, S.; Schmid, P.; Mayr, S. Xylem Sap Surface Tension May Be Crucial for Hydraulic Safety. *Plant Physiology* **2017**, *175*, 1135–1143.

(13) Majewski, J.; Kuhl, T.; Kjaer, K.; Smith, G. Packing of Ganglioside-Phospholipid Monolayers: An X-Ray Diffraction and Reflectivity Study. *Biophysical Journal* **2001**, *81*, 2707–2715.

(14) Frey, S. L.; Chi, E. Y.; Arratia, C.; Majewski, J.; Kjaer, K.; Lee, K. Y. C. Condensing and Fluidizing Effects of Ganglioside GM1 on Phospholipid Films. *Biophysical Journal* **2008**, *94*, 3047–3064.

(15) Ingram, S.; Salmon, Y.; Lintunen, A.; Hölttä, T.; Vesala, T.; Vehkamäki, H. Dynamic Surface Tension Enhances the Stability of Nanobubbles in Xylem Sap. *Frontiers in Plant Science* **2021**, *12*.

(16) Watanabe, M.; Netzer, F.; Tohge, T.; Orf, I.; Brotman, Y.; Dubbert, D.; Fernie, A. R.; Rennenberg, H.; Hoefgen, R.; Herschbach, C. Metabolome and Lipidome Profiles of Populus × canescens Twig Tissues During Annual Growth Show Phospholipid-Linked Storage and Mobilization of C, N, and S. *Frontiers in Plant Science* **2018**, *9*.

(17) Marsh, D. *Handbook of Lipid Bilayers*; CRC Press, 2013.

(18) Kirkwood, J. G.; Buff, F. P. The Statistical Mechanical Theory of Surface Tension. *The Journal of Chemical Physics* **1949**, *17*, 338–343.

(19) Tempra, C.; Ollila, O. H. S.; Javanainen, M. Accurate Simulations of Lipid Monolayers Require a Water Model with Correct Surface Tension. *Journal of Chemical Theory and Computation* **2022**, *18*, 1862–1869.

(20) Abascal, J. L. F.; Vega, C. A general purpose model for the condensed phases of water: TIP4P/2005. *The Journal of chemical physics* **2005**, *123*, 234505.

(21) Wang, Z.-J.; Frenkel, D. Pore nucleation in mechanically stretched bilayer membranes. *The Journal of Chemical Physics* **2005**, *123*, 154701.

(22) Kanduč, M.; Schneck, E.; Loche, P.; Jansen, S.; Schenk, H. J.; Netz, R. R. Cavitation in lipid bilayers poses strict negative pressure stability limit in biological liquids. *Proceedings of the National Academy of Sciences* **2020**, *117*, 10733–10739.

(23) Cochard, H.; Barigah, T.; Herbert, E.; Caupin, F. Cavitation in plants at low temperature: Is sap transport limited by the tensile strength of water as expected from Briggs' Z-tube experiment? *New Phytologist* **2007**, *173*, 571–575.

(24) Olżyńska, A.; Zubek, M.; Roeselova, M.; Korchowiec, J.; Cwiklik, L. Mixed DPPC/POPC Monolayers: All-atom Molecular Dynamics Simulations and Langmuir Monolayer Experiments. *Biochimica et Biophysica Acta - Biomembranes* **2016**, *1858*, 3120–3130.

(25) Menzl, G.; Gonzalez, M. A.; Geiger, P.; Caupin, F.; Abascal, J. L.; Valeriani, C.; Dellago, C. Molecular mechanism for cavitation in water under tension. *Proceedings of the National Academy of Sciences of the United States of America* **2016**, *113*, 13582–13587.

(26) Rayleigh, L. VIII. On the pressure developed in a liquid during the collapse of a spherical cavity. *The London, Edinburgh, and Dublin Philosophical Magazine and Journal of Science* **1917**, *34*, 94–98.

(27) Plesset, M. S. The Dynamics of Cavitation Bubbles. *Journal of Applied Mechanics* **1949**, *16*, 277–282.

(28) Lei, Y. A.; Bykov, T.; Yoo, S.; Zeng, X. C. The Tolman Length: Is It Positive or Negative? *Journal of the American Chemical Society* **2005**, *127*, 15346–15347.

(29) Tanaka, K. K.; Tanaka, H.; Angélil, R.; Diemand, J. Simple improvements to classical bubble nucleation models. *Physical Review E* **2015**, *92*, 022401.

(30) Ollila, O. H. S.; Lamberg, A.; Lehtivaara, M.; Koivuniemi, A.; Vattulainen, I. Interfacial Tension and Surface Pressure of High Density Lipoprotein, Low Density Lipoprotein, and Related Lipid Droplets. *Biophysical Journal* **2012**, *103*, 1236–1244.

(31) Kashchiev, D. Nucleation work, surface tension, and Gibbs–Tolman length for nucleus of any size. *The Journal of Chemical Physics* **2020**, *153*, 124509.

(32) Guan, X.; Schenk, H. J.; Roth, M. R.; Welti, R.; Werner, J.; Kaack, L.; Trabi, C. L.; Jansen, S. Nanoparticles are linked to polar lipids in xylem sap of temperate angiosperm species. *Tree Physiology* **2022**,

(33) Christensen-Dalsgaard, K. K.; Tyree, M. T.; Mussone, P. G. Surface tension phenomena in the xylem sap of three diffuse porous temperate tree species. *Tree Physiology* **2011**, *31*, 361–368.

(34) Lee, J. et al. CHARMM-GUI Membrane Builder for Complex Biological Membrane Simulations with Glycolipids and Lipoglycans. *Journal of Chemical Theory and Computation* **2019**, *15*, 775–786.

(35) Harris, J. G.; Yung, K. H. Carbon Dioxide's Liquid-Vapor Coexistence Curve And Critical Properties as Predicted by a Simple Molecular Model. *The Journal of Physical Chemistry* **1995**, *99*, 12021–12024.

(36) Vujić, B.; Lyubartsev, A. P. Transferable force-field for modelling of CO2, N2, O2 and Ar in all silica and Na+ exchanged zeolites. *Modelling and Simulation in Materials Science and Engineering* **2016**, *24*, 045002.

(37) Abraham, M. J.; Murtola, T.; Schulz, R.; Páll, S.; Smith, J. C.; Hess, B.; Lindahl, E. GROMACS: High performance molecular simulations through multi-level parallelism from laptops to supercomputers. *SoftwareX* **2015**, *1-2*, 19–25.

(38) Nosé, S. A unified formulation of the constant temperature molecular dynamics methods. *The Journal of Chemical Physics* **1984**, *81*, 511–519.

(39) Parrinello, M.; Rahman, A. Polymorphic transitions in single crystals: A new molecular dynamics method. *Journal of Applied Physics* **1981**, *52*, 7182–7190.

(40) Duncan, S. L.; Larson, R. G. Comparing Experimental and Simulated Pressure-Area Isotherms for DPPC. *Biophysical Journal* **2008**, *94*, 2965–2986.

(41) Wang, X.; Binder, K.; Chen, C.; Koop, T.; Pöschl, U.; Su, H.; Cheng, Y. Second inflection point of water surface tension in the deeply supercooled regime revealed by entropy anomaly and surface structure using molecular dynamics simulations. *Physical Chemistry Chemical Physics* **2019**, *21*, 3360–3369.

(42) Hess, B.; Bekker, H.; Berendsen, H. J. C.; Fraaije, J. G. E. M. LINCS: A linear constraint solver for molecular simulations. *Journal of Computational Chemistry* **1997**, *18*, 1463–1472.

(43) McGibbon, R. T.; Beauchamp, K. A.; Harrigan, M. P.; Klein, C.; Swails, J. M.; Hernández, C. X.; Schwantes, C. R.; Wang, L.-P.; Lane, T. J.; Pande, V. S. MDTraj: A Modern Open Library for the Analysis of Molecular Dynamics Trajectories. *Biophysical Journal* **2015**, *109*, 1528–1532.

(44) Gonzalez, M. A.; Abascal, J. L. F.; Valeriani, C.; Bresme, F. Bubble nucleation in simple and molecular liquids via the largest spherical cavity method. *The Journal of Chemical Physics* **2015**, *142*, 154903.

(45) Dehaoui, A.; Issenmann, B.; Caupin, F. Viscosity of deeply supercooled water and its coupling to molecular diffusion. *Proceedings of the National Academy of Sciences* **2015**, *112*, 12020–12025.

TOC Graphic